Article

Not peer-reviewed version

Towards Real-Time Railroad Inspection Using Directional Eddy Current Probe

Meirbek Mussatayev * and Mohammed Alanesi

Posted Date: 15 April 2024

doi: 10.20944/preprints202402.1075.v2

Keywords: Eddy current testing; lift-off; real-time inspection; probe optimization; signal-to-noise ratio

 doi:10.20944/preprints202402.1075.v2

Article

Towards Real-Time Railroad Inspection Using Directional Eddy Current Probe

Meirbek Mussatayev [1,‡,*] and Mohammed Alanesi [2]

[1] Affiliation Department of Mechanical Engineering, Ultrasonics and Non-destructive Testing (UNDT), University of Bristol, Bristol, BS8 1TR, UK; Meirbek.Mussatayev@bristol.ac.uk
[2] Department of Intelligent Manufacturing Engineering, Guilin University of Electronic Technology, Guilin, 541004, China; alanesi@guet.edu.cn
* Correspondence: Meirbek.Mussatayev@bristol.ac.uk;
† Current address: Beacon House, Queens Rd, Bristol BS8 1QU, UK.
‡ These authors contributed equally to this work.

Abstract: In the field of railroad safety, effective detection of surface cracks is critical, necessitating reliable, high-speed non-destructive testing (NDT) methods. This study introduces a hybrid Eddy Current Testing (ECT) probe, specifically engineered for railroad inspection, to address the common issue of 'lift-off noise' due to varying distances between the probe and test material. Unlike traditional ECT methods, this probe integrates transmit and differential receiver coils, aiming to enhance detection sensitivity and minimize lift-off impact. The study optimizes ECT probes employing different driver coils, emphasizing three main objectives: a) quantitatively evaluating each probe using signal-to-noise ratio (SNR) and outlining a real-time data processing algorithm based on SNR methodology; b) exploring the frequency range proximal to the electrical resonance of the receiver coil; c) examining sensitivity variations across varying lift-off distances. The experimental outcomes indicate that the newly designed probe with figure 8-shape driver coil significantly improves sensitivity in detecting surface cracks on railroads. It achieves an impressive SNR exceeding 100 for defects with minimal dimensions of 1 mm in width and depth. Simulation results closely align with experimental findings, validating the investigation of optimal operational frequency and lift-off distance for selected probe performance, determined to be 0.3 MHz and 0.5 mm, respectively. The realization of this project would lead to notable advancements in enhancing railroad safety by improving crack detection efficiency.

Keywords: Eddy current testing; lift-off; real-time inspection; probe optimization; signal-to-noise ratio.

1. Introduction

Non destructive testing (NDT) plays a crucial role in ensuring the safety and reliability of engineering structures across various sectors, including automotive, aerospace, and civil engineering. A critical component in the railway system is the railway track, which is susceptible to various types of cracks. Current standards for railway inspection predominantly rely on visual testing (VT) methods, which are time-consuming, qualitative, and the VT remain limited by top surface inspection and the need for expertise. Monitoring surface and sub-surface defects, including burns, squat-like rail cracks, and others type of local damages costs for the millions of pounds every year in U.K. [1,2] railway inspection and capability of real-time inspection of these defects presents significant challenges, with only a limited array of NDT techniques available. Among these, Ultrasonic Testing (UT) is frequently utilized due to its ability to penetrate the bulk material of the track, particularly in the rail head and web. However, this technique encounters a notable limitation in identifying both surface and subsurface anomalies smaller than 4 mm in depth during high-speed inspections [3,4]. While it is possible to detect surface imperfections through the reflective echoes of ultrasonic waves once they reach a particular size, UT is not capable of assessing the extent of these defects nor can it differentiate among various defect categories [5]. Thus, there is an urgent need for a more efficient and reliable surface and sub-surface inspection method to ensure structural integrity of rail tracks. Consequently, ECT has been identified as an appropriate NDT technique for in-line railway inspection. To realize this application and facilitate full automation of the inspection process, the integration of various

 doi:10.20944/preprints202402.1075.v2

distinct technologies is imperative. This integration is essential to address the complex requirements of real-time, efficient, and accurate railway inspection. This project aims to significantly enhance efficiency by implementing real-time on-train inspection technology, as illustrated in Figure 1. The primary challenge in measurements of this nature is not inherently linked to the limitations of sensor technology but rather pertains to the management and processing of the data collected [6].

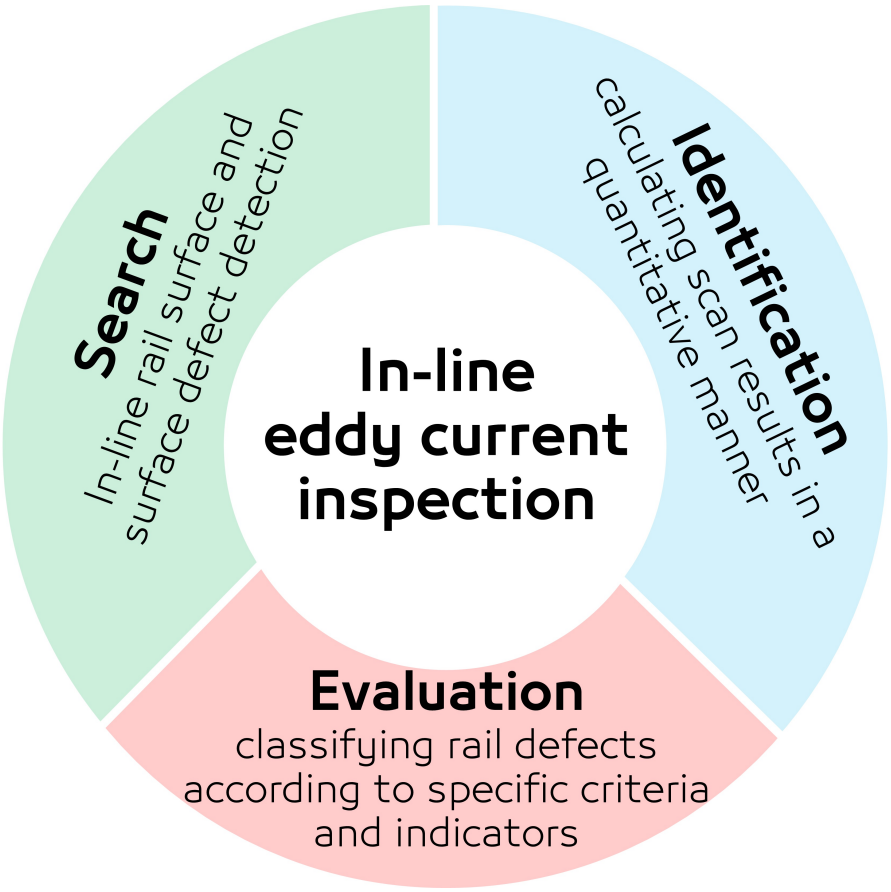

Figure 1. Improved efficiency of current railroad inspection.

There were many attempts to embed the similar EC systems for online detection and location of rails defects published before [7–9]. However, the lack of available EC probe optimization studies for real-time inspection [10], coupled with the need for improved data management options, motivates the present investigation. Specific online data processing algorithm is provided to manage with the huge amount of data effectively associated with the nature of this type of inspection. During each inspection, the system aboard the train accumulates a substantial volume of data, within which only a fraction is of significant relevance. Identifying and extracting these pertinent data segments is crucial for determining their precise locations along the track. Typically, specialized research groups are dedicated to the management of such data, employing strategies that involve either transmitting the data for remote analysis or conducting local analysis onboard to detect anomalies that surpass predefined thresholds. Despite the fact that based on the proposed improved system as is shown in Figure 1 this project needs to characterize the different types of actual types of railroads damages this initial research is limited to search and identification parts.

This initial research aims to optimize the proposed ECT probe designs to develop inspection system integrated within on-train inspection technology, capable for real-time inspection in dynamic conditions. Further studies will be more focused on investigation the characterization of localized rail track defects, particularly quats. The goal is to optimize the sensor design, enhancing its sensitivity to these specific defects under varying inspection conditions, including factors like speed and vibration.

 doi:10.20944/preprints202402.1075.v2

Another challenge posed by strongly ferromagnetic steels in ECT, particularly in the context of rail steels with high coercivity. Compelling instances of overcoming this challenge are demonstrated through the development of ECT probes for numerous rail inspection systems [11–13], encompassing both ECT and UT [14–16] as well as integrated ECT on-train inspection technologies [17–19]. To address the issue of defect detection, the finite element method was applied to predict the detectability of targeted defects using high coercivity soft iron material as the core. In [20], authors tested conventional transmit-receive EC sensors for simulated rail defect detection, highlighting challenges in extracting defect-modulated signals. They found that the detection coil's output is predominantly influenced by direct induced voltage from the excitation coil, making it difficult to discern voltage variations caused by defect-induced EC changes buried within the large baseline signal. Additionally, variations in the distance between the sensor and the rail due to vibrations and bumping introduce a "lift-off" effect, further complicating defect characterization. In response to these challenges, the study has developed a new hybrid ECT probe, tailored to fulfill the unique requirements of real-time, accurate rail track inspection. A substantial body of research has been dedicated to the optimization of EC probes, with various studies focusing on enhancing their efficacy in diverse applications. In an exploration of the efficacy of ECT for in-plane fiber waviness detection in unidirectional carbon fiber reinforced plastic (CFRP), [21] employed a diverse set of probes: circular driving, symmetrical driving, and uniform driving. This study is distinguished by its methodical comparative analysis and the integration of sophisticated image processing techniques, including the Canny filter and Hough transform, to ascertain the probes' precision and accuracy against X-ray CT imaging benchmarks. The research notably identifies the uniform driving probe as superior in accurately detecting fiber waviness angles above 2° in unidirectional CFRP, evidenced by a root mean square error of 1.90° and a standard deviation of 4.49°. However, the study's applicability may be constrained by its focused examination of specific waviness angles and CFRP types. Expanding on ECT probe optimization, [22] investigates the Near Electrical Resonance Signal Enhancement (NERSE) phenomenon. This study reveals that operating an absolute EC probe near its electrical resonance, particularly in the 1 to 5 MHz frequency range, significantly amplifies defect signals in aerospace superalloy Titanium 6Al-4V. The research reports signal-to-noise ratio (SNR) peaks up to 3.7 times higher near resonance frequencies, attributed to defect-induced resonant frequency shifts. This finding posits a straightforward yet efficacious approach to enhancing the sensitivity of standard industrial EC testing through the NERSE frequency band. In the realm of real-time EC inspection, [23] focuses on giant magnetoresistive (GMR) field sensors, juxtaposing finite-element model (FEM) predictions with experimental findings to underscore the development of a swift and flexible inspection system. Concurrently, [24] details the optimization of a low-frequency EC technique for internal defect detection in steel structures, analyzing a custom-designed magnetic sensor system in tandem with FEM results. This study explores the fine-tuning of probes using magnetoresistive sensors, supported by simulations with CIVA software.

In [25] delineates the development of a flexible planar EC sensor array, targeting microcrack inspection in critical airplane components. The study details the sensor design, measurement mechanics, and correlates these with FEM outcomes.

In a significant advancement, in [26] present a differential coupling double-layer coil for ECT, achieving notable improvements in sensitivity and lift-off tolerance. This coil's innovative double-layer structure and differential coupling energy mechanism demonstrate the potential of strategic coil design and frequency optimization in overcoming traditional limitations of EC probe sensitivity, especially in scenarios with high lift-off. An extended literature review about applications and advantages of planar rectangular receiver in ECT provided in this study. Further progress is reported in [27], which proposes a novel figure 8-shaped coil for transmitter-receiver (T-R) probes. This unique design effectively counters signal distortion due to lift-off variation and maintains consistent output when aligned with the CFRP's fiber orientation. The probe is characterized by its insensitivity to lift-off variations and enhanced sensitivity to defects in CFRPs. Lastly, authors in [28] present an analytical model for a figure 8-shaped coil comprising two oblique elliptical coils. This model enables the manipulation of

 doi:10.20944/preprints202402.1075.v2

the electromagnetic concentrative region and the EC density. Adjustments in the elliptical shape or the spread angle between the coils lead to intensified and expanded eddy currents (ECs), concentrating under the coil's symmetric center. This innovative design and analytical methodology significantly elevate the accuracy in detecting conductive material defects, marking a pivotal development in NDT methods. While each study substantially enriches the field of ECT probe optimization and NDT, their practical application varies based on specific conditions, material types, and defect characteristics. These advancements lay the groundwork for exploring the applicability of novel EC probes in railroad inspection. The objective of this paper is the development of ECT sensors tailored for real-time surface inspection of rail tracks, exploring design parameters of a novel directional ECT probe for detecting surface-breaking cracks and common railway flaws. This research, aimed at optimizing EC probes presented in [29], seeks to significantly enhance real-time inspection effectiveness, potentially marking a break-through in railroad inspection methodologies.

The development of the proposed inspection system, as depicted in Figure 1, necessitates comprehensive studies to verify the feasibility and reliability of integrating the probe into the real-time on-train inspection technology. This integration must account for variations in speed and vibrations from both the train and rail tracks, necessitating probe optimization. However, the current experimental setup is primarily aimed at optimizing the probe design for heightened sensitivity to common defects in ferromagnetic materials, rather than replicating the exact operational environment. The directional probe design previously outlined in references [21] has not yet been

tested on metallic components. Studies in [21,29,30] have demonstrated optimum sensitivity beyond the receiver's resonance for CFRP materials, which now requires validation for ferromagnetic materials. Therefore, our methodology involves multiple studies focusing on real-time EC probe optimization. This research utilizes the SNR for quantitative evaluation, comparing the sensitivity of the best probe configuration from earlier research [29] with the two novel sensor designs proposed in this study. Investigating the optimal frequency is crucial for boosting sensitivity to specific defects. This study delves into the proximity frequency range, resonating the receiver coil to elevate SNR levels. Similar research [6] analyzed phase shifts with frequency variations to identify the optimal operational frequency, noting that increased phase shifts improve defect depth resolution and decrease detection errors. Another critical aspect of this research is determining the optimal lift-off distance, ranging from 0.25 to 1 mm, as lift-off variation is a key parameter before in-situ inspection.

This involves balancing sensitivity against lift-off distance, an essential factor in EC probe optimization. Related research [7] conducted fixed-distance (1 mm) inspections from the rail track surface by integrating EC instrumentation into a grinding train for early detection of surface damages. This highlights the importance of understanding the trade-offs between sensitivity and lift-off distance for effective EC probe deployment in real-world applications.

1.1. Sensor Design

The paper presents a frequency selection study focusing on three sensor designs, depicted in Figure 2. To minimise the lift off noise differentially winded two adjacent rectangular sensors and to increase the induced ECs density and concentrative area within the material single driver, special figure 8-shape elliptical and four figure 8-shape (+point) driver coils were designed and manufactured. The initial design utilizes singular excitation driver coils, while subsequent modifications involve altering the aspect ratio of the previous non-uniform configuration [29], as depicted in Figure 2(a), tailored for the inspection requirements of railroad infrastructure. Drawing upon principles from EC theory, the inclusion of winding +point [6]] and 8-shape [27] configurations aims to amplify the sensitivity of pickup signals. However, it is noteworthy that similar driver designs have not been previously manufactured to enhance the sensitivity of EC probe for the specific needs of the targeted application.

 doi:10.20944/preprints202402.1075.v2

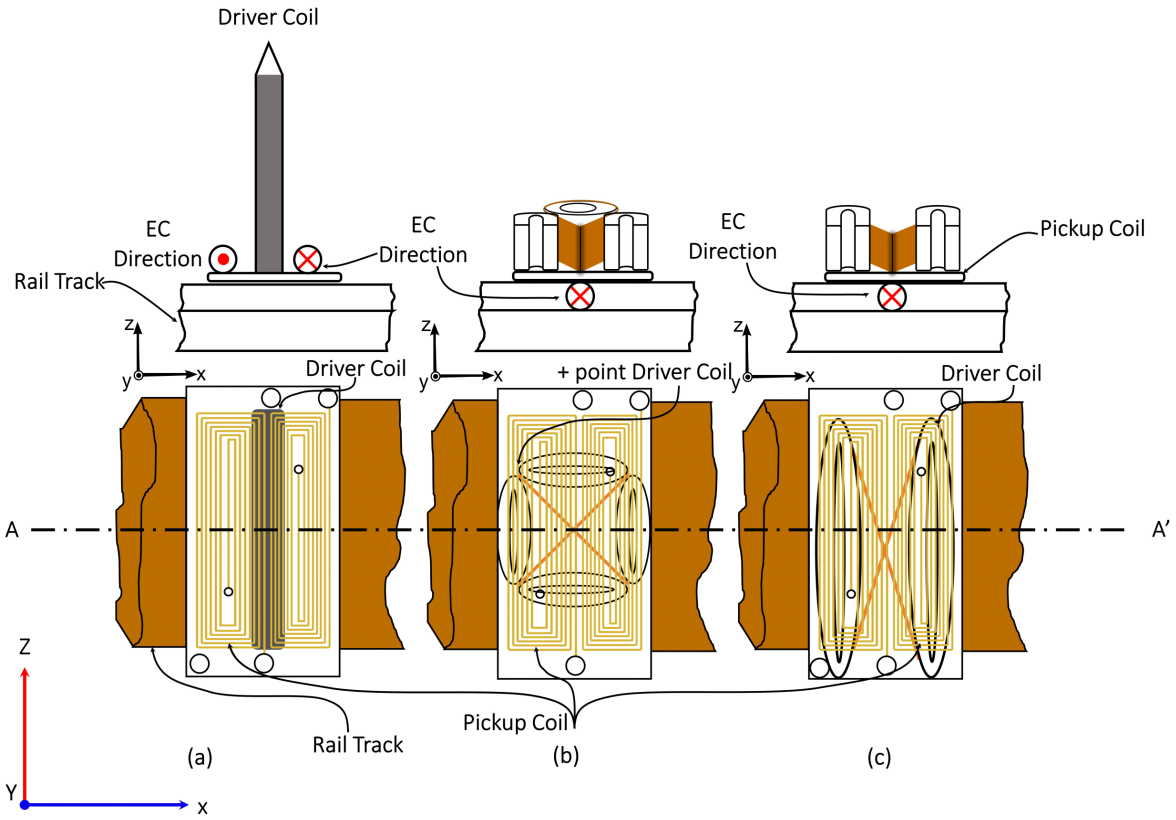

Figure 2. Three eddy current probe configurations with: (a) singular; (b) +point and (c) figure 8-shape

1.2. Driver Coil Design

To optimize performance under the distributed magnetic field of the driver coil, the width of the coil recommended to be equal or exceed the length of the pickup coil. Increasing the number of turns in the driver coil strengthens the magnetic field but raises inductance, consequently lowering resonance frequency. The fabrication of driver coils with 62, 72, and 66 turns on ferrite, corresponding to single, +point, and 8-shape configurations, respectively, ensures the generation of a suitably robust magnetic field to produce the desired excitation frequency signal. Table 1 provides driver and pickup coils parameters. Peak frequencies of the driver coil vary based on winding quality and turn count. Figure 3(a-c) shows +point, 8-shape and single winding methods along with their dimensions and resonance frequencies, respectively. The driver coils' impedance spectra were assessed employing a Network Analyzer (TE3001, Trewmac Systems, Australia). Resonant frequencies of approximately 1.1, 0.6, and 1 MHz were observed for the single, +point, and figure 8-shape drivers, respectively.

Table 1. Material properties and dimensions of the driver coil.

Driver coil name	Parameters and dimensions
Single	62 turns, 0.5 mm diameter, 38X27X5.5 mm
+point	72 turns, 0.2 mm diameter, 18X5X8 mm
Figure 8-shape	66 turns, 0.2 mm diameter, 40X12X6.5 mm

Preprints.org (www.preprints.org) | NOT PEER-REVIEWED | Posted: 15 April 2024 doi:10.20944/preprints202402.1075.v2

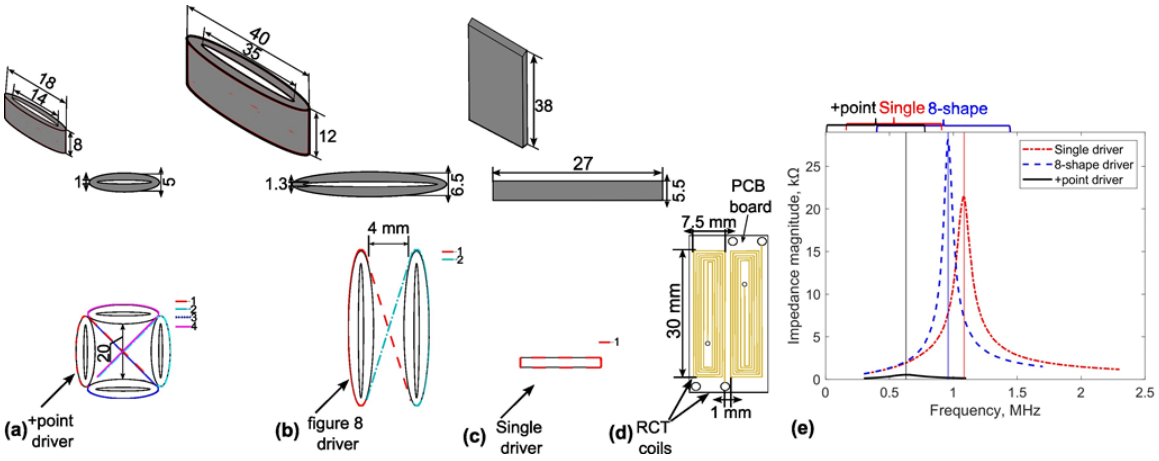

Figure 3. Directional EC probe design: (a) winding method of the +Point, (b) figure 8-shape, (c) rectangular single drivers, (d) rectangular (RCT) pickup coil dimensions (top-down view) and resonant frequencies of different driver coils.

1.3. Planar Rectangular Pickup Coils

The planar rectangular pickup coils advantages and some limitations along with its application challenges is reviewed by study in [26]. The consistency of detected signals and the flexibility to manufacture with various dimensions to accommodate for different track widths make printed PCB-based technology ideal candidate for manufacturing. The sensor parameters and dimensions are presented in Table 2 and Figure 3(d) respectively.

Table 2. Material properties and dimensions of the sensing coil.

Receiver coils	Parameters and dimensions
Number of turns	12
Product Family	2 layer
Copper Weight	35
Thickness	1.6mm
Material	FR4 (150 deg C) middle Tg
Circuit Size X	30 mm

1.4. Amplifier

In ECT NDE, limitations arise from noise sources like sample electromagnetic property variations, vibration, temperature changes, and probe lift-off and tilt. Utilizing SNR as a metric for probe performance evaluation is advisable. Figure 4 illustrates the fundamental components of the amplifier and the coil input circuits. The low-pass filtering effect of the feedback amplifiers is characterized by the closed-loop bandwidth, which is the unity gain-bandwidth product divided by the closed-loop gain. While further reducing bandwidth at a specific gain value is feasible, it introduces phase lags at target frequencies, impacting gain. In the simplified circuit diagram, all external circuitry is situated left of the "Input 1" & "Input 2" terminals, with onboard components to their right. Coils L1 & L2 function as pickup coils, inducing emfs in series opposition, yielding a differential voltage output. L3 and L4, the drive coils, wound in a "figure of eight" pattern around ferrite bar cores, generate opposing AC fields at adjacent poles. The drive coil tuning capacitor, chosen for resonance, amplifies coil currents and voltages, enhancing sensitivity and SNR. The combined output of the pickup coils serves as a differential input signal for the amplifier, connected to Input 1 & 2 terminals. The input circuit features switch-selectable capacitors for coil tuning and various loading resistors, with the option to disconnect the center ground connection. Implementing a non-earth referenced input via a

 doi:10.20944/preprints202402.1075.v2

signal isolation transformer is preferred, offering cost-effective common mode rejection. The amplifier circuit, inclusive of the isolation transformer, delivers a gain of 10 (or +20 dB) into an infinite resistance load, with a flat frequency response between 100kHz and 2MHz. Beyond 5MHz, gain reduces to 19.3 dB with a 40° phase lag, with a 3dB drop at 11.25MHz. For remote signal transmission, 50 ohm coaxial cable is advised, with a 50 ohm termination for cables longer than approximately 3 meters, typically reducing gain by 6dB. Capacitor switchers were integrated into the amplifier board to adjust the receiver coil's resonant frequency within a specified range. Equation 1 provides a formula for calculating the required capacitance for desired resonance based on probe coil inductance and target frequency.

$$C = \frac{1}{\omega_0{}^2 L} \tag{1}$$

where $\omega_0 = 2\pi f_0$. Here, f_0 represents the desired resonant frequency (1.5 MHz), C is the tuning capacitance in farads, and L denotes the probe inductance (1.0×10^{-6} H). The signal-to-noise ratio (SNR) quantifies the proportion of the desired signal to the level of background noise. It is a pivotal metric in the evaluation of system performance, particularly in the context of signal processing.

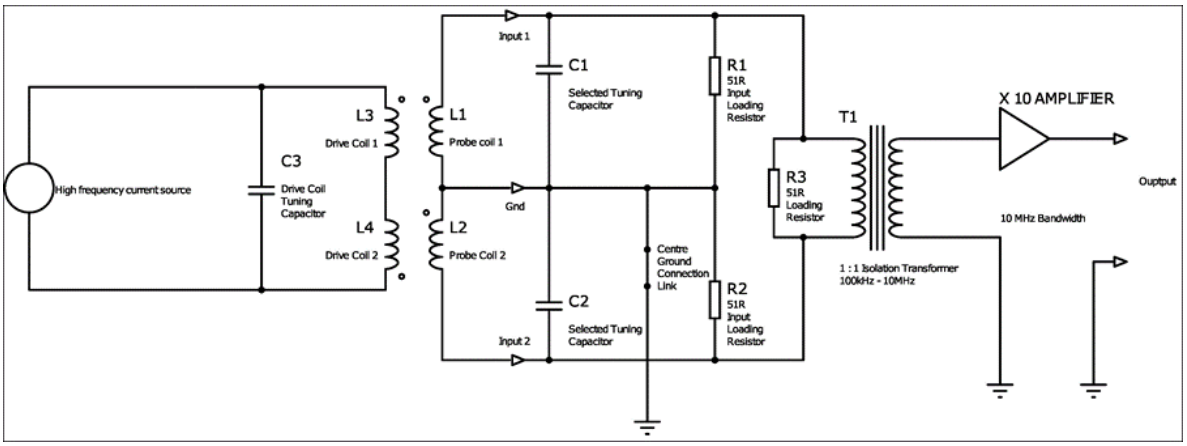

Figure 4. Simplified diagram of amplifier with tuning caps and drive coils.

1.5. Methodology for Estimating SNR

The evaluation of three probe design sensitivities and identification section in Figure 1 is quantitatively assessed using SNR. Figure 5 depicts the proposed methodology for identification based on a 0.4MHz exemplar sensor signal using an EC probe with a figure 8-shaped driver coil. Data collection begins from 0 to 50 mm over a large non-damaged area of the rail track (as shown in Figure 5). This data is utilized for automatic calculation of twice the root-mean-squared (RMS) value of background structural noise as a threshold to distinguish sensor signals (indicated by the horizontal dashed line in Figure 5). Any signal exceeding twice the mean RMS noise voltage is considered a sensor signal and undergoes peak value detection. Upon passing the defective zone, the algorithm automatically provides information about the estimated SNR calculated using the equation 2:

$$SNR = \frac{V_{\max} + |V_{\min}|}{2N_{\text{rms}}} \tag{2}$$

where $V_{\max}$ represents the maximum observed signal voltage, $V_{\min}$ denotes the minimum observed signal voltage, and N_{rms} is the root mean square value of the noise level. Here, the signal-to-noise ratio (SNR) quantifies the proportion of the desired signal to the level of background noise and is a pivotal metric in the evaluation of system performance, particularly in the context of signal processing.

 doi:10.20944/preprints202402.1075.v2

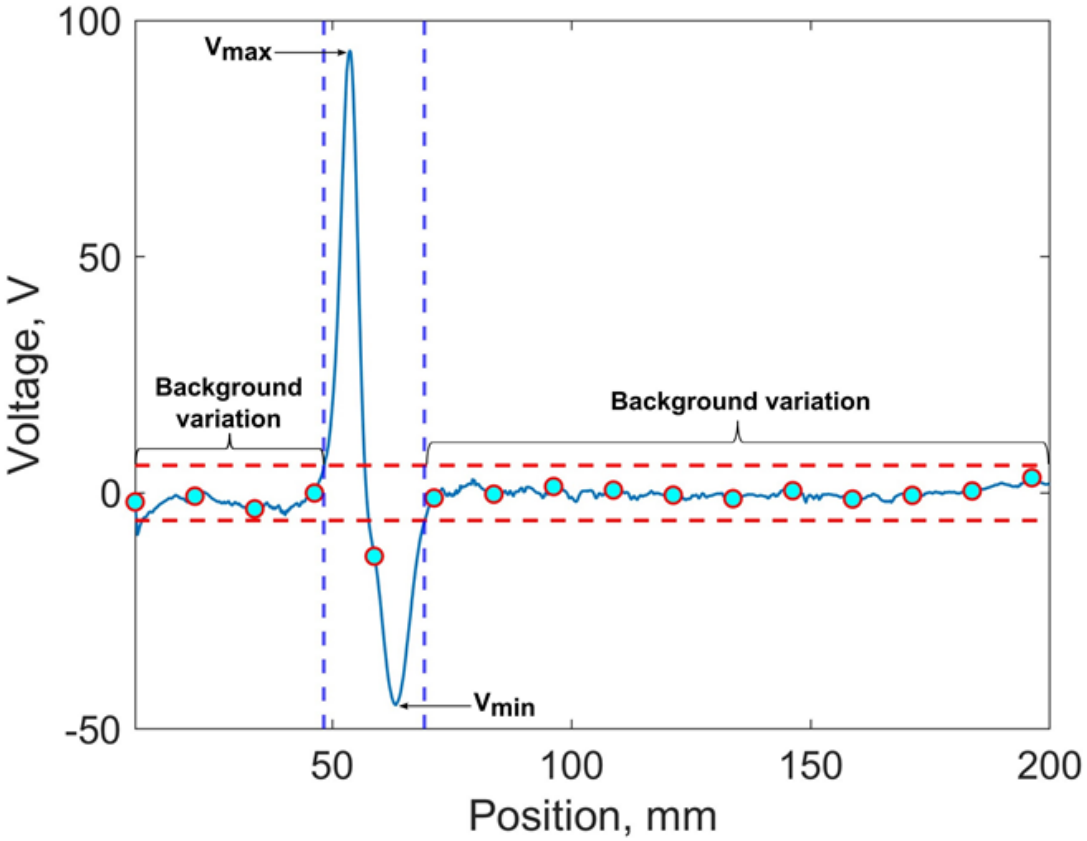

Figure 5. Exemplar plot of identification process of proposed system.

1.6. Finite Element Modelling of Three Probe Configurations

A comprehensive finite element modeling (FEM) investigation was executed employing COMSOL 6.1. The simulation speed was carefully calibrated to balance computational efficiency and accuracy, which is critical for practical applications. The study leveraged insights from Chen et al. [26], utilizing a differential coupling double-layer coil approach to enhance testing capabilities, especially in high lift-off scenarios.

1.7. Modeling Method

The virtual scanning model was executed employing COMSOL 6.1, as meticulously illustrated in Figure 6. The model spans the x-axis from -20 mm to 20 mm, encompassing both the defective area (ranging from -0.5 mm to 0.5 mm) and the surrounding non-defective zones, which exhibit structural variations. The detailed FEM setup parameters are presented in Table 3.

 doi:10.20944/preprints202402.1075.v2

Table 3. Finite element modeling setup parameters.

Parameters	Singular Probe	Plus-Point Probe	Figure-8 Probe
Driver coil dimensions, mm	27x5.5x38	18x5x8	40x6.5x12
Driver wire diameter, mm	0.5	0.2	0.2
Driver coil turns	62	72	66
Pick up coil turns		12 turns	
Pick up coil dimensions, mm		30 x 7.5 x 1	
Pick up coil thickness		3.4 mm	
Gap between two pick-up coils	1 mm	1 mm	1 mm
Pick up coil wire diameter, mm		0.2	
Lift-off distance, mm		0.25	
Core material		Soft Iron	
Physics setting in COMSOL		Magnetic fields	
FEM study steps		Study 1: Coil Geometry Analysis	
		Study 2: Frequency Domain Study	

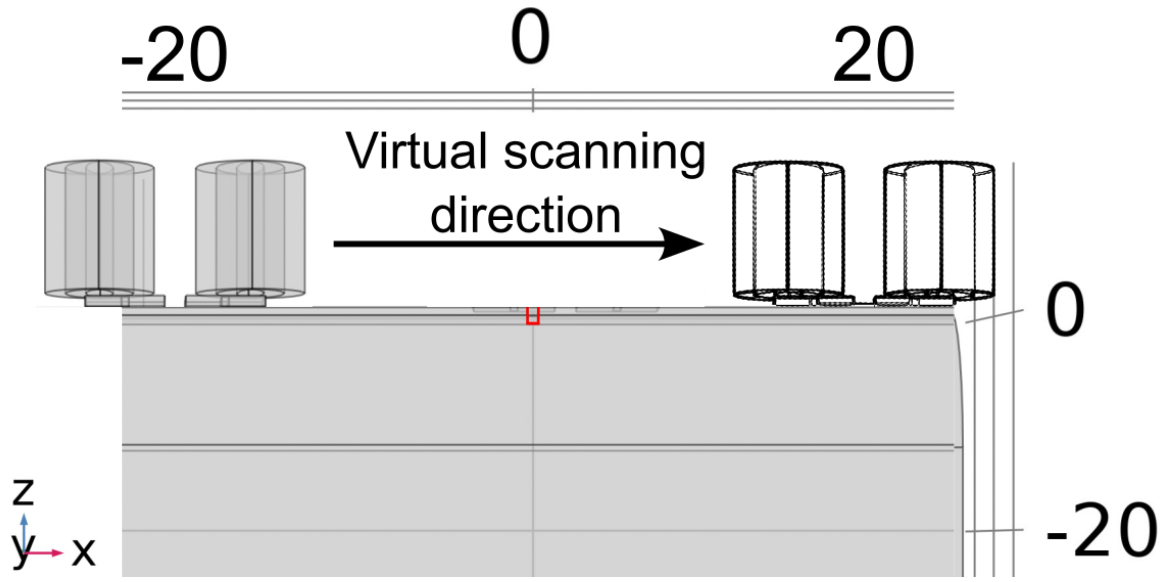

Figure 6. Schematic of the virtual scanning model.

1.8. Probe Configuration Analysis

Figure 7.i presents a detailed FEM mesh overview, showcasing the air domain and driver coils in the 'Singular,' '+Point,' and 'Figure-8' configurations, along with a close-up of the driver coils positioned adjacent to the rail defect. The induced ECs generated by the 'Singular', '+Point', and 'Figure-8' configurations are illustrated in Figures 7.ii.(a)-(c), respectively. Notably, all configurations drive currents non-uniformly, and the EC probe with the figure-8 shape driver exhibits the most intense ECs density among the others. This can be attributed to the fact that the figure-8 shape transmitter coil generates ECs driven between increased elliptical factor of both ferrites, inducing significant current densities in areas of the defect, as evidenced in Figure 7.ii.(c), thereby reducing structural influences. In contrast, the ECs densities in Figure 7.ii.(d), resulting from the +point driver configuration, suggests that this probe is better suited to be rotated into a -45-degree orientation to improve its detection capabilities.

Preprints.org (www.preprints.org) | NOT PEER-REVIEWED | Posted: 15 April 2024 doi:10.20944/preprints202402.1075.v2

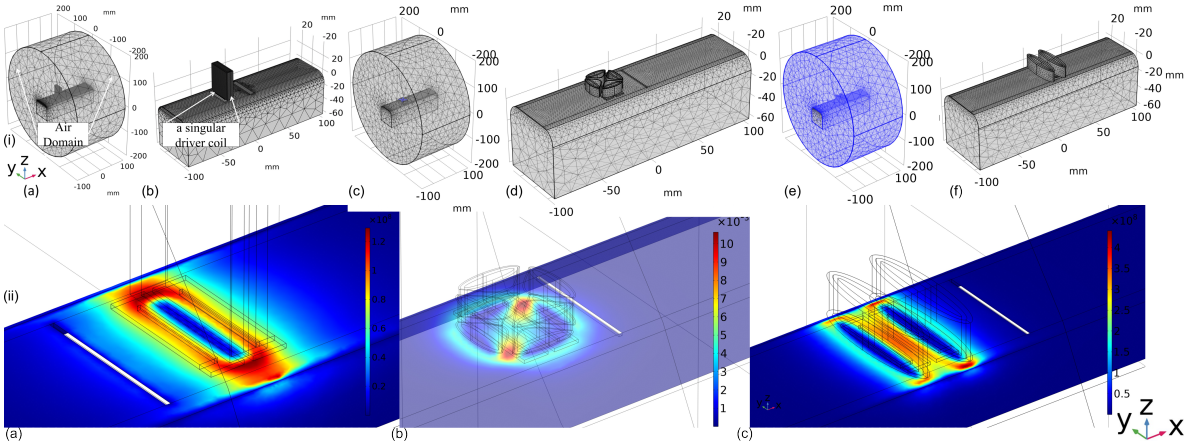

Figure 7. (i) Simulated mesh overview: (a), (c), and (e) show the mesh with the air domain, while (b), (d), and (f) provide a zoom-in view of the driver coils' positioning near the rail for the 'Singular', '+Point', and 'Figure-8' configurations, respectively. (ii) FEM simulations of induced eddy current flow patterns for (a) singular, (b) plus-point, and (c) figure-8-shaped probes.

2. Experiments

2.1. Rail Track with Induced Artificial Defect

A series of sore cuts introduced on the top surface of rail track specimen for proposed inspection system's optimization study as is shown in Figure 8(a). The material of the sample is made from the standard R260 grade rails. The probe capabilities can be evaluated best by inspecting one artificial defect over the relatively large non-defected area. The dimensions of sore cut are 40x1.0x0.8 mm.

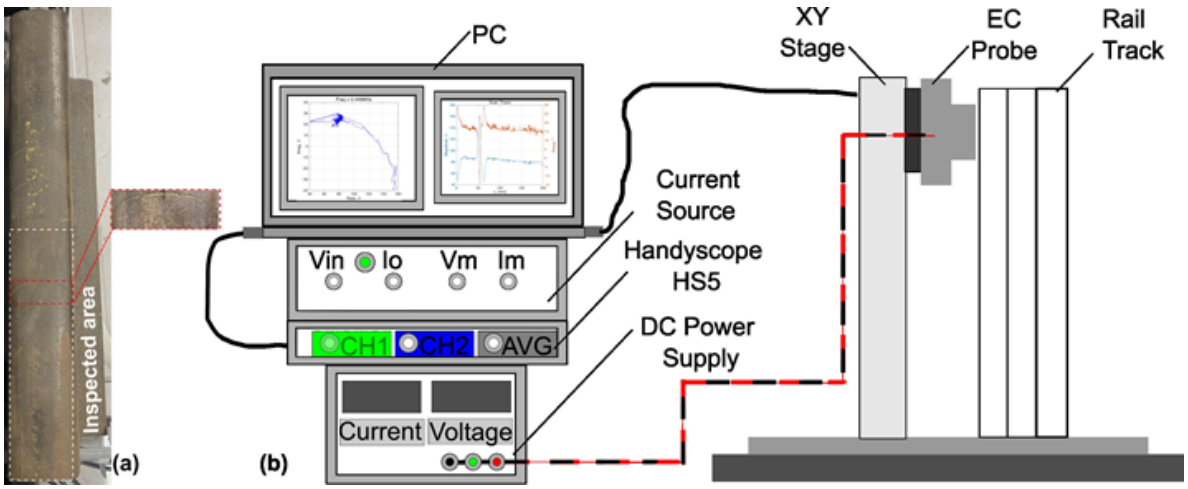

Figure 8. a) Experimental set-up b) Rail track sample.

2.2. Measurement Set-up

The experimental set-up is illustrated in Figure 8b. The main magnetic field generated by the driver coil induces ECs within the rail track sample, resulting in the generation of a secondary magnetic field. The secondary magnetic fields, which vary over time, cause a voltage to be induced in the pickup coils. The presence of a near-surface defect on the rail disrupts the local distribution of the ECs, causing a slight alteration in the induced voltage detected by the coil. The set-up comprises an handyscope (TiePie Engineering) generating a sinusoidal signal, linked to a Holland current source (Sonemat) and the DC power supply HY 3003. One output from the current source supplies a consistent current to the driver coil for magnetic field excitation. The other output is connected to the handyscope to serve as a stable voltage reference for voltage difference comparison with received pick up signals from the

 doi:10.20944/preprints202402.1075.v2

probe. The power supply provides a ±9.5 V DC supply to the differential amplifier. Real-time control and post-processing of measurements are handled by a MATLAB script interfacing the handyscope with the computer.

3. Results

3.1. Frequency Selection Study

The experimental setup involved conducting at least three repeated independent measurements across a 200 mm range for each specimen to enhance precision in real-time using MATLAB. The movement increment was set at 0.125 mm, resulting in a maximum of 1600 data points. The collected data underwent post-processing to detrend signal amplitudes, followed by smoothing using MATLAB's built-in filtering, and subsequent calculation of the SNR. Further details on post-processing methods can be found in Appendix A1 of Ref. [7].

The experimental investigation into optimum frequency selection for EC probes utilized frequency ranges of 0.2÷0.7 MHz with a single driver, 0.4÷1.3 MHz with a +point driver, and 0.15÷0.6 MHz with a figure 8-shape driver with 0.35 V to drive the driver coil. The selection of frequency ranges was influenced by observed noise levels. Higher frequency ranges near the resonant frequency of the pickup coil were avoided due to challenges posed by factors such as magnetic hysteresis, complex microstructure, and high permeability in ferromagnetic materials, except for the EC probe with the +point driver. Optimizing EC probes necessitates careful control of factors affecting measurement noise levels and adjustment of the resonant frequency. Capacitors of 10 nF were used to tune the pickup coil's resonant frequency, each coil having an inductance of approximately 1µH, tuned for resonance at the operational frequency. Specific resonant frequency could be achieved by calculating the required capacitance using Equation 1. The sensor signals obtained from FEM simulations exhibit variations compared to the experimental data. This discrepancy may be attributed to differences in the inspection speed applied during FEM simulations. Given that the speed is beyond the scope of this study, it will be considered in subsequent investigations for result comparison. In each row, Figure 9 (i) displays the raw EC data for each probe configuration and (ii) shows simulated corresponding differential voltage outputs. Discrepancies are observed, particularly in the clear differences in sensor signal shape and absolute voltage value for the figure-8 shape driver coil. These discrepancies arise because the simulation study relied on a higher coercivity material, as referenced in Table 3. The accurate experimental parameters have not been precisely retrieved, which is currently under investigation. Figure 10 illustrates SNR estimation outcomes around the sensor coil resonant frequency, demonstrating improved signal strength and reduced uncertainty across various frequency ranges. All scan positions except those marked by the vertical dashed lines are used as undamaged sections of the structural background rail to assess the RMS of noise for each measurement. To evaluate the probe performance, the mean RMS noise value is multiplied by two to establish the noise threshold level (indicated by the horizontal dashed line in Figure 9 i.(a)-(c)). Among the probes, the one with the Figure 8-shape driver exhibited the lowest structural noise value, while the nonuni90o probe showed the highest. Among the three EC probes, the figure 8-shape configuration outperformed the other two, nearly triple the SNR, with the maximum SNR recorded at 105 at 0.25 MHz. The EC probe with the single driver exhibited real-time inspection capability, achieving an SNR of approximately 13 at 0.5 MHz, while the +point driver probe doubled the performance, achieving around 27 SNR at 0.6 MHz. Further investigation into varying lift-off distances and their impact on ECT sensitivity will focus on the probe with the figure 8-shape configuration.

Preprints.org (www.preprints.org) | NOT PEER-REVIEWED | Posted: 15 April 2024 doi:10.20944/preprints202402.1075.v2

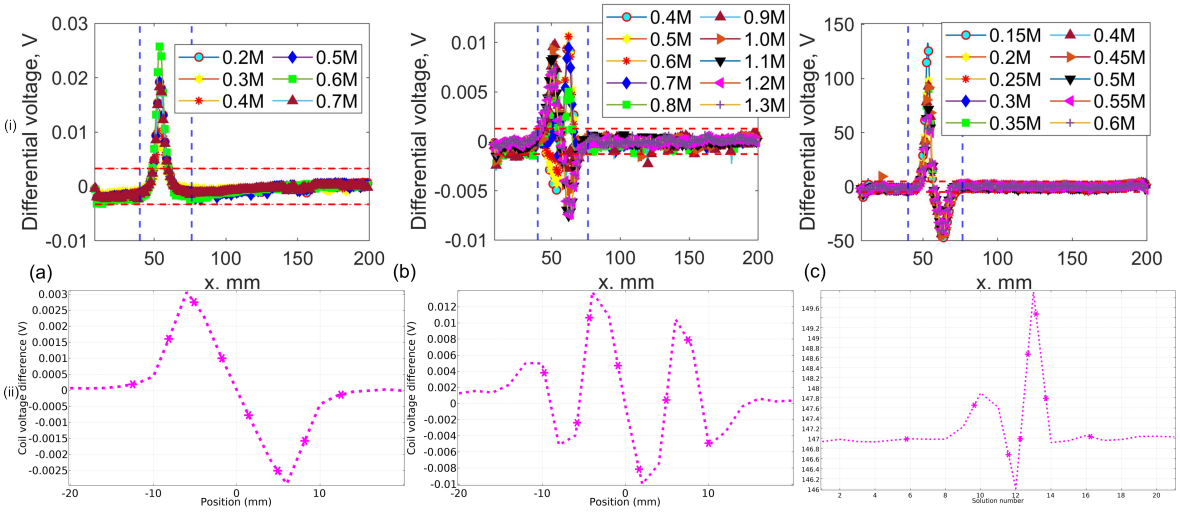

Figure 9. Optimal frequency selection study results depicted in rows: i) experimental raw EC data; ii) FEM simulations for EC probes with driver coils in configurations: a) single, b) plus-point, and c) figure-8 shape.

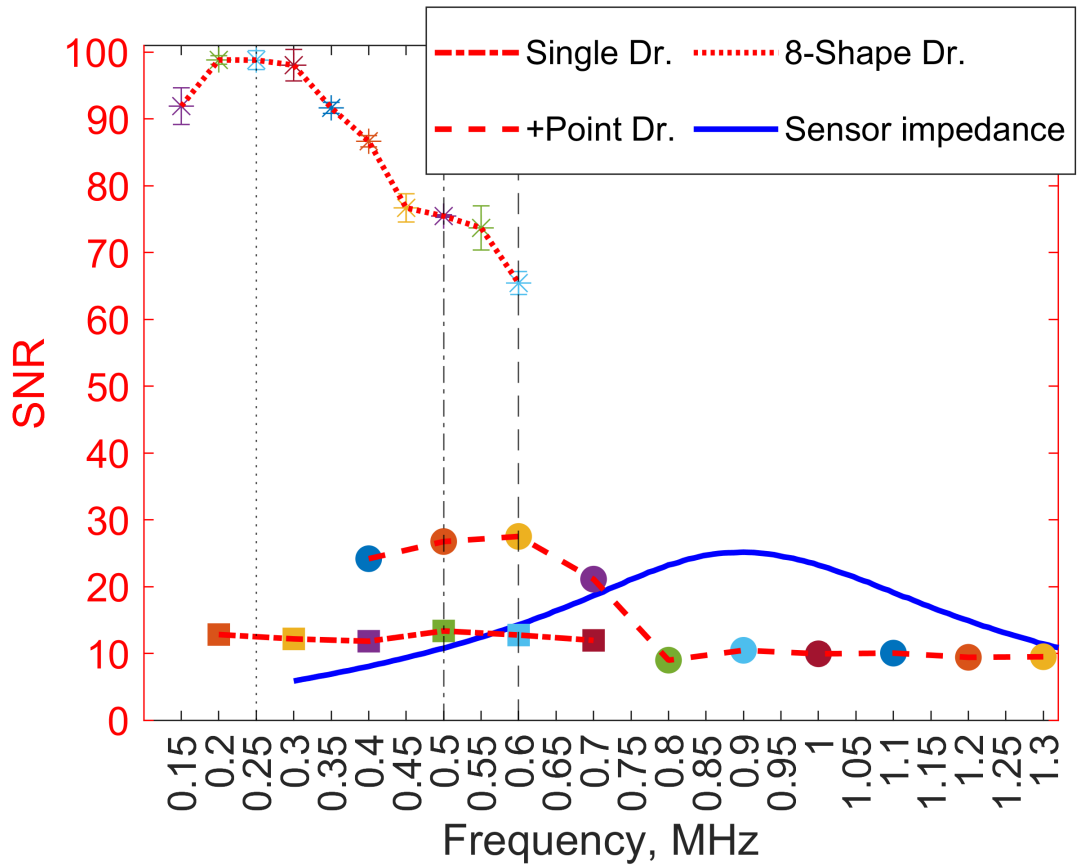

Figure 10. Comparative analysis of probe sensitivity across various frequency ranges

3.2. Lift-off Distance and Optimum Probe Sensitivity

Understanding a selected probe's sensitivity to targeted defects, particularly concerning variations in lift-off distance, is crucial before implementing the sensor in real-world settings. Previous studies consistently maintained a 0.25 mm distance across all measurements. However, in [7] the research applied sensor integration in a similar environment with a 1 mm lift-off distance. Therefore, to explore

 doi:10.20944/preprints202402.1075.v2

probe sensitivity across a range of 0.25 to 1 mm, a minimum of three independent measurements were conducted, varying both frequency and lift-off distance. The rationale for maintaining a constant frequency range was to evaluate the noise level at different lift-off distances. This approach is critical for future studies, where the integration of this probe configuration might be necessary under varying operational frequencies. MATLAB software was utilized to ensure real-time accuracy in data acquisition and analysis. Figure 11 presents the selected probe sensitivity profile, demonstrating its differential voltage response as a function of varying lift-off distances. A notable trend observed was a significant decrease in the recorded differential voltage as the distance from the rail surface increased within the range of 0.5 to 1 mm. To facilitate a quantitative comparison and assess the individual contributions of influential factors such as signal and coherent structural noise, the raw EC data presented in Figure 11 underwent further post-processing, following the methodology described by [29].

The SNR and RMS of structural noise were analyzed across varying lift-off (LO) distances for the selected probe performance at different frequencies, as shown in Figure 12. (a). At a lift-off distance of 0.5 mm, the SNR reached its peak at approximately 105. However, it is worth noting that the uncertainty represented by the error bars was relatively higher compared to those observed at the 0.25 mm lift-off distance, as depicted in Figure 12(b). At 0.3 MHz, the SNR exhibited a gradual increase across all three distances, indicating enhanced SNR. This trend coincided with relatively lower levels of structural noise observed at this optimal frequency. At the 1 mm lift-off distance, the lowest SNR values with higher uncertainty were recorded after the 0.4 MHz frequency. The observed phenomenon was attributed to the higher levels of coherent noise observed between 0.4 MHz and 0.6 MHz as is demonstrated in Figure 12.(a). Commencing at the upper frequency ranges of 0.35-0.6 MHz, a notable decline in SNR of the selected probe was observed for all lift-off distance ranges, as depicted in Figure 12.(b). Even when the lift-off distance was increased to 1 mm, the probe exhibited the lowest sensitivity in terms of voltage magnitude (see Figure 11.(c)), yet it maintained a relatively high SNR between 40-77. The mean SNR, signal voltage values from three lift-off distance measurements were analyzed, along with the root mean square (RMS) noise associated with each, and plotted as a function of lift-off distance at a frequency of 0.3 MHz, as illustrated in Figure 12.(c). The obtained results indicate that, in contrast to the peak-to-peak signal voltage, structural noise emerges as the most influential factor contributing to the observed high level of sensitivity. These results indicate that the EC probe featuring a figure-8-shaped driver demonstrates a relatively high voltage magnitude at a lift-off distance of 0.5 mm and a frequency of 0.3 MHz. Notably, this configuration maintains excellent detection sensitivity, with a signal-to-noise ratio (SNR) exceeding 100, within a specific lift-off range.

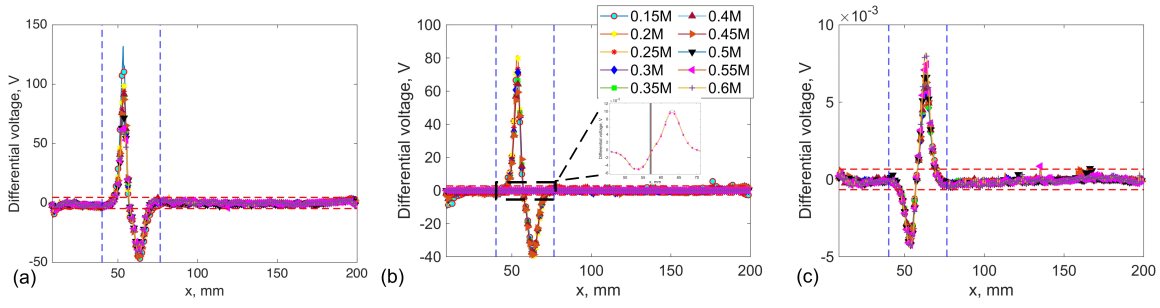

Figure 11. Eddy current scan data captured with a figure-8-shaped driver at lift-offs of a) 0.25 mm, b) 0.5 mm, and c) 1 mm.

 doi:10.20944/preprints202402.1075.v2

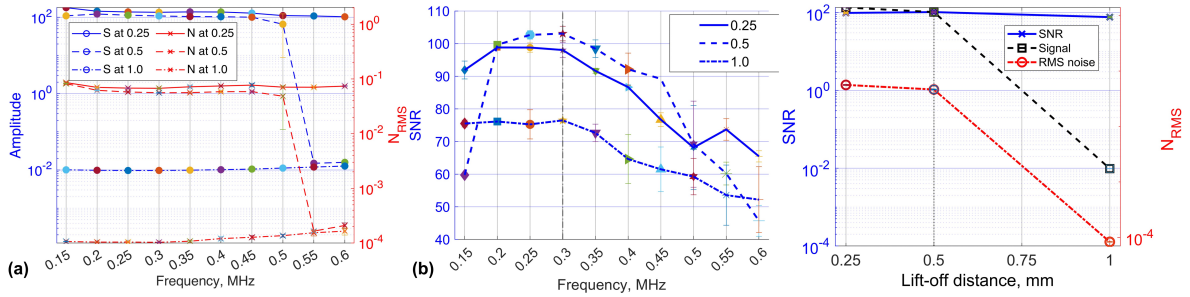

Figure 12. Performance assessment of EC probe with a figure-8-shape driver across lift-off distances of 0.25 mm, 0.5 mm, and 1.0 mm: a) signal (S) and noise (N) separate contribution and b) SNR across various frequencies; c) average voltage and structural noise at optimum 0.3 MHz.

3.3. Experimental Validation of Probe Sensitivity for Local Rail Damage

To assess the performance of the selected EC probe with a figure 8-shape driver for artificial local defects, a steel plate of the same grade was fabricated. The specimen, measuring 155mm x 80mm x 21mm, featured five drilled holes with a diameter of 1 mm, positioned as depicted in Figure 13. Three initial defects, situated from the left edge as illustrated in Figure 13, were examined at operational frequencies of 0.25, 0.3, and 0.35 MHz. Due to the arrangement of receivers in a differential EC mode with a width of 7.5 each, the sensor signals from the initial holes were symmetrical as shown in Figure 14. However, with a distance of 9 mm between each hole, subsequent scans covered the other two defects simultaneously. Moving further, sensors placed over the first and second holes yielded pickup signals that, when overlapped over the defective zone, formed the first half of an "M" shape sensor signal. Subsequently, scanning over the third defect completed the second half of the "M" shape sensor signals.

 doi:10.20944/preprints202402.1075.v2

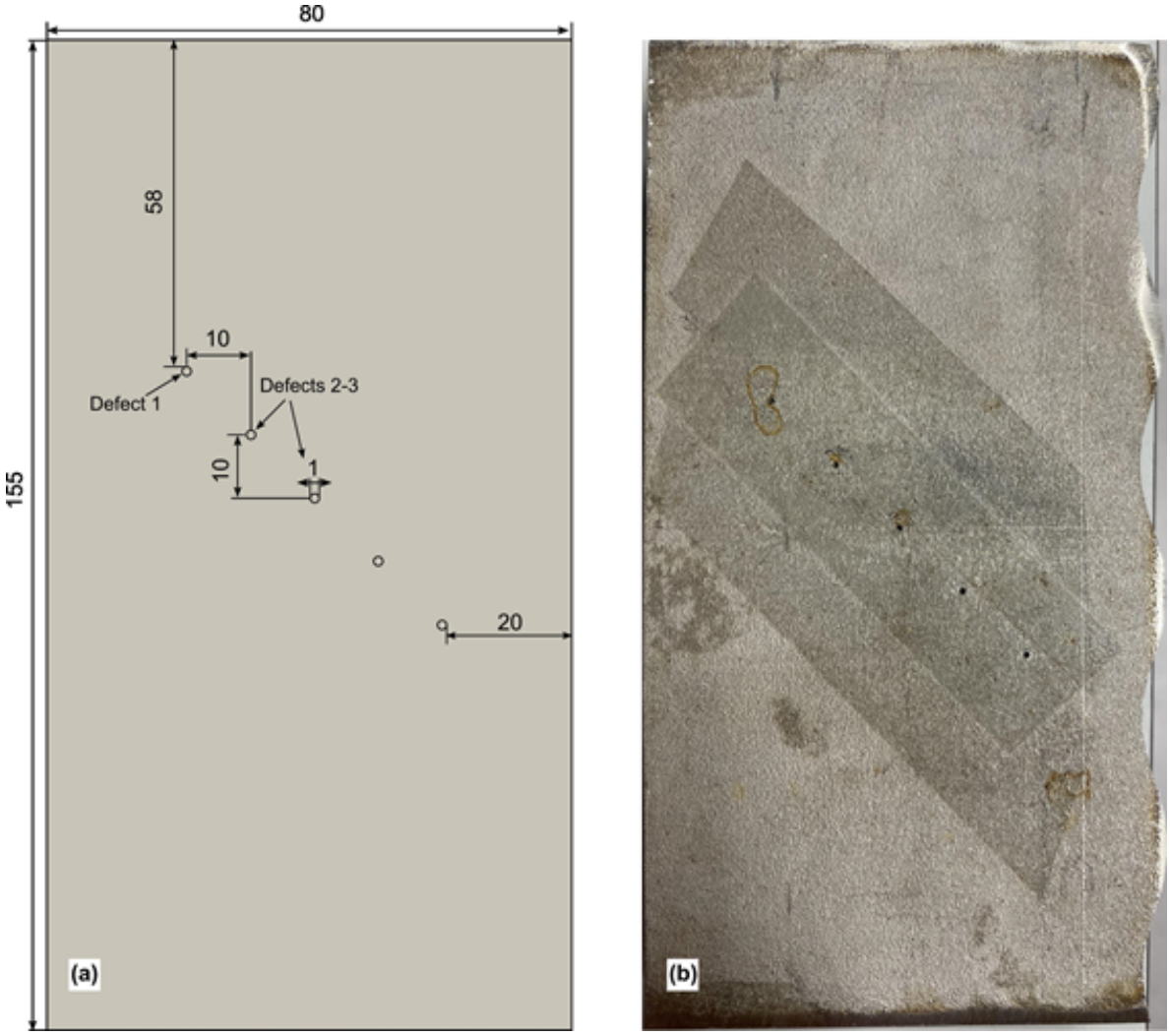

Figure 13. Dimensions of the specimen and artificially drilled hole: a) schematic diagram; b) real photo of the specimen.

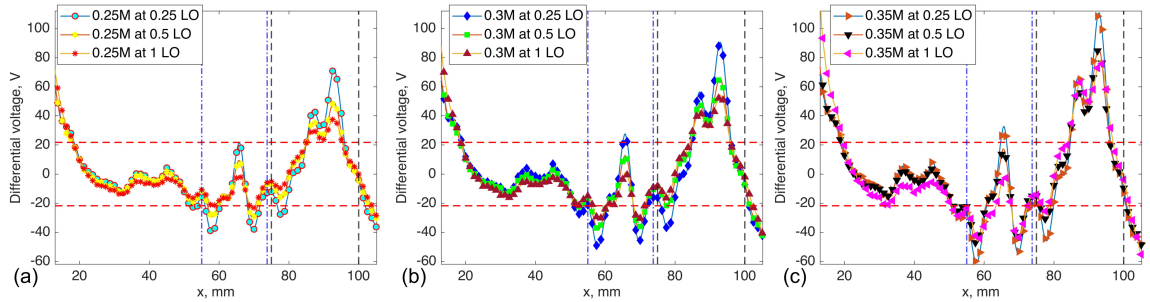

Figure 14. Raw EC data with lift-off distances of 0.25, 0.5, and 1 mm at: a) 0.25 MHz, b) 0.3 MHz, and c) 0.35 MHz operational frequencies.

The sensitivity of the selected probe during scanning over each defect, along with its estimated SNR and the contribution of structural noise, were evaluated independently, as depicted in Figure 15. The estimated structural noise was relatively higher due to edge effects, resulting in lower SNR. Despite the noise level, the selected probe exhibited slightly better performance around 0.35 MHz, achieving SNRs of 7.5 and 12.5 for the 1st and 2-3rd defects, respectively.

 doi:10.20944/preprints202402.1075.v2

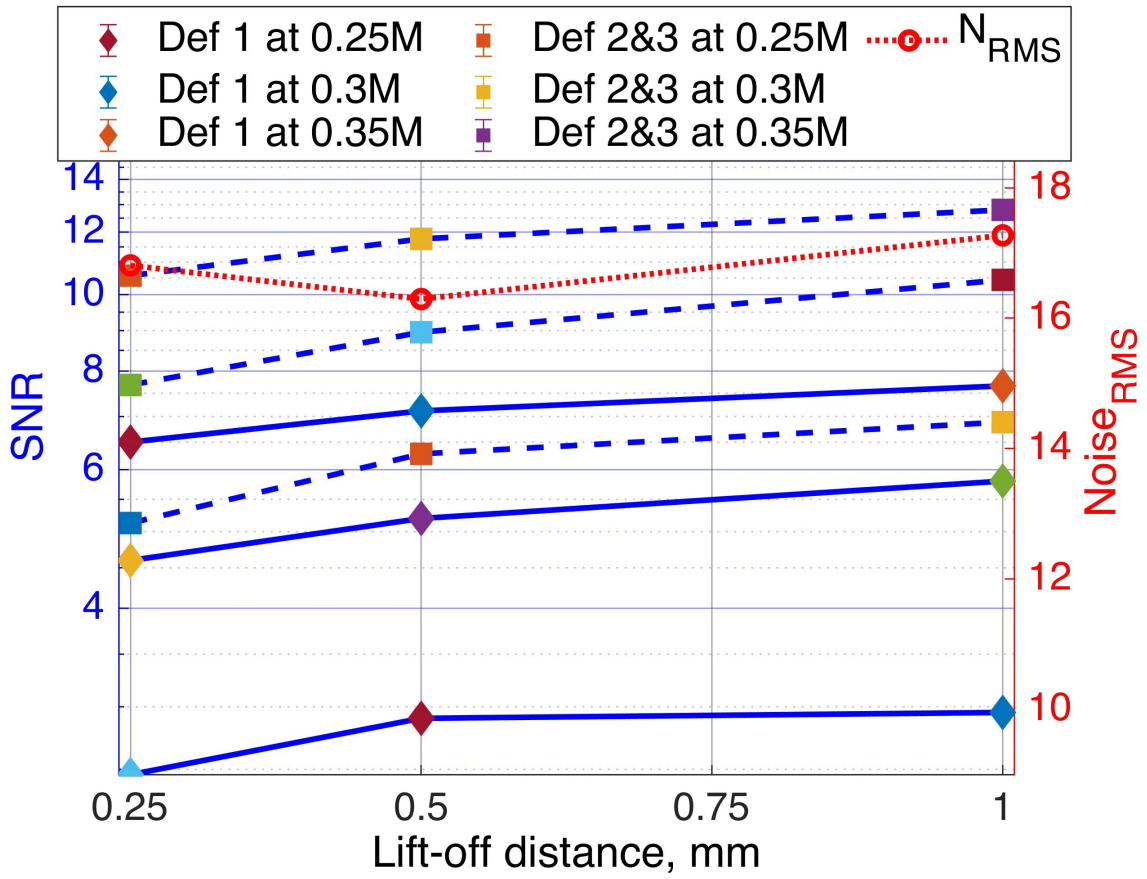

Figure 15. Selected probe Signal-to-Noise Ratio over defect 1 and defects 2-3, with separate noise contributions as a function of lift-off distance.

4. Conclusions

The study explored various combinations of excitation coil designs in conjunction with a rectangular planar receiver coil, assessing their potential integration into on-train inspection technology for a real-time, high-speed, and reliable rail track inspection. The sensitivity of detection as a function of lift-off was also scrutinized. It was concluded that detectability could be enhanced using a figure-8-shaped driver coil at a frequency of 0.3 MHz, while maintaining a lift-off distance of around 0.5 mm. The results from both case studies indicated that the Tx-Rx sensor exhibits superior SNR in detecting ferromagnetic material structures. Measurements revealed that ferromagnetic material structures are more readily detected at relatively low frequencies (0.3MHz), facilitating in-line electronics and data acquisition. The probe with the figure-8-shaped driver coil demonstrated optimal SNR near the resonant frequency peak of the pickup coil. The enhanced inspection system represents an innovative and fundamentally promising application, closely aligning with the criteria requisite for integration in Industry 4.0. To fully harness the potential of this advanced inspection system and optimize its use, it is imperative to include real rail track defect characterization and demonstrate its effectiveness in detecting manufacturing flaws in authentic environments. Consequently, future work will involve validating the effectiveness of a new EC instrument, integrated into a special inspection handcart at the Scunthorpe plant of British Steel. This future research will focus on detecting squats and other localized types of damage.

Meirbek Mussatayev is affiliated with the Department of Mechanical Engineering and Ultrasonics and Non-destructive Testing (UNDT) at the University of Bristol, U.K. He holds a Ph.D. from the Guilin University of Electronic Technology, China. He earned his B.Sc. and M.Sc. degrees in Automation and Control and Mechanical Engineering from the Academy of Logistics and Transport, Kazakhstan, and Tomsk Polytechnical University, Russia, in 2009 and 2013, respectively. His research focuses on dimensional

 doi:10.20944/preprints202402.1075.v2

metrology and eddy current non-destructive testing. His career as a metrology engineer spans over 10 years across various sectors, including national metrology institutes, GPS calibration laboratories, geophysical centers, and verification and calibration of measuring devices in major energy projects.

Mohammed Alanesi is an Associate Professor at Guilin University of Electronic Technology in China. He earned his B.Sc. in Communication and Electronic Engineering from Applied Science Private University, Jordan, and completed his Ph.D. in Mechanical Engineering at Guilin University of Electronic Technology. Dr. Alanesi's research primarily focuses on triboelectric nanogenerators (TENG) and their application in enhancing IoT for smart environments. Renowned for his expertise in electronic design and programming, he is deeply committed to advancing research and education in mechanical engineering and nanotechnology.

Acknowledgments: I extend my sincere gratitude to my supervisors, R. Hughes and P. Wilcox, for their invaluable suggestions and guidance. Special thanks are due to Prof R. Lewis from Sheffield University, U.K., for his expert advice. Additionally, I acknowledge the financial support provided by the Bolashak International Scholarship, Kazakhstan, which enabled my research in this field.

Author Contributions: For research articles with several authors, a short paragraph specifying their individual contributions must be provided. The following statements should be used "Conceptualization, M.M.; methodology, M.M.; software, M.M.; validation, M.M.; FEM analysis, M.A.; investigation, M.M.; resources, M.M.; data curation, M.M.; writing—original draft preparation, M.M.; writing FEM section—editing, M.A.; visualization, M.M.; supervision, M.M.; project administration, M.M.; funding acquisition, M.M. All authors have read and agreed to the published version of the manuscript.

References

1. Y. Muhamedsalih, S. Hawksbee, G. Tucker, J. Stow, and M. Burstow, "Squats on the Great Britain rail network: Possible root causes and research recommendations," Int. J. Fatigue, vol. 149, no. April, p. 106267, 2021, doi: 10.1016/j.ijfatigue.2021.106267.
2. D. F. Cannon, K. Edel, S. L. Grassie, and K. Sawley, "Rail defects: an overview RAILS, STRESSES, RAIL FAILURE AND COSTS," pp. 865–886, 2003.
3. L. Xiong, G. Jing, J. Wang, X. Liu, and Y. Zhang, "Detection of Rail Defects Using NDT Methods," Sensors, vol. 23, no. 10, 2023, doi: 10.3390/s23104627.
4. J. Peng, G. Y. Tian, L. Wang, Y. Zhang, K. Li, and X. Gao, "Investigation into eddy current pulsed thermography for rolling contact fatigue detection and characterization," NDT E Int., vol. 74, pp. 72–80, 2015, doi: 10.1016/j.ndteint.2015.05.006.
5. Q. Li and S. Ren, "A real-time visual inspection system for discrete surface defects of rail heads," IEEE Trans. Instrum. Meas., vol. 61, no. 8, pp. 2189–2199, 2012, doi: 10.1109/TIM.2012.2184959.
6. S. G. Kwon, T. G. Lee, S. J. Park, J. W. Park, and J. M. Seo, "Natural rail surface defect inspection and analysis using 16-channel eddy current system," Appl. Sci., vol. 11, no. 17, 2021, doi: 10.3390/app11178107.
7. R. Pohl, R. Krull, D. B. Ag, R. Meierhofer, and S. I. Sa, "A new Eddy Current Instrument in a Grinding Train," pp. 1–7, 2006.
8. A. Dey, H.-M. Thomas, and R. Pohl, "The Important Role of Eddy Current Testing in Railway Track Maintenance," p. 4, 2008.
9. T. A. Alvarenga, A. L. Carvalho, L. M. Honorio, A. S. Cerqueira, L. M. A. Filho, and R. A. Nobrega, "Detection and Classification System for Rail Surface Defects Based on Eddy Current," pp. 1–15, 2021.
10. A. N. Abdalla, M. A. Faraj, F. Samsuri, D. Rifai, and K. Ali, "Challenges in improving the performance of eddy current testing: Review," 2018, doi: 10.1177/0020294018801382.
11. Z. Song, T. Yamada, H. Shitara, and Y. Takemura, "Detection of Damage and Crack in Railhead by Using Eddy Current Testing," J. Electromagn. Anal. Appl., vol. 03, no. 12, pp. 546–550, 2011, doi: 10.4236/jemaa.2011.312082.
12. J. Wang, Q. Dai, P. Lautala, H. Yao, and R. Si, "Rail Sample Laboratory Evaluation of Eddy Current Rail Inspection Sustainable System," Sustain., vol. 14, no. 18, pp. 1–22, 2022, doi: 10.3390/su141811568.
13. Z. Liu, A. D. Koffman, B. C. Waltrip, and Y. Wang, "Eddy Current Rail Inspection Using AC Bridge Techniques," J. Res. Natl. Inst. Stand. Technol., vol. 118, p. 140, 2013, doi: 10.6028/jres.118.007.
14. H. M. Thomas, T. Heckel, and G. Hanspach, "Rail: Advantage of a combined ultrasonic and eddy current examination for railway inspection trains," Insight Non-Destructive Test. Cond. Monit., vol. 49, no. 6, pp. 341–344, 2007, doi: 10.1784/insi.2007.49.6.341.

15. T. Heckel, H. M. Thomas, M. Kreutzbruck, and S. Rühe, "High speed non-destructive rail testing with advanced ultrasound and eddy-current testing techniques," NDT Prog. 2009 - 5th Int. Work. NDT Expert. Proc., no. May 2014, pp. 101–109, 2009.
16. B. Rockstroh et al., "Ultrasonic and Eddy-Current Inspection of Rail Wheels and Wheel Set Axles," 17th World Conf. Nondestruct. Test., no. January, pp. 25–28, 2008.
17. J. W. Park et al., "Rail Surface Defect Detection and Analysis Using Multi-Channel Eddy Current Method Based Algorithm for Defect Evaluation," J. Nondestruct. Eval., vol. 40, no. 3, pp. 1–12, 2021, doi: 10.1007/s10921-021-00810-9.
18. P. Chandran, M. Rantatalo, J. Odelius, H. Lind, and S. M. Famurewa, "Train-based differential eddy current sensor system for rail fastener detection," Meas. Sci. Technol., vol. 30, no. 12, 2019, doi: 10.1088/1361-6501/ab2b24.
19. S. Rail, D. House, and R. T. C. Business, "A Pedestrian and Vehicle-Mounted System for Detecting RCF in Rail using Eddy Currents," 19th World Conf. Non Destr. Test., pp. 1–9, 2016.
20. Z. Liu, W. Jia, L. Zhu, and X. Zhang, "Rail defect inspection using alternating current excitation coils with digital demodulation algorithm," Conf. Rec. - IEEE Instrum. Meas. Technol. Conf., pp. 235–238, 2011, doi: 10.1109/IMTC.2011.5944142.
21. H. Kosukegawa, Y. Kiso, M. Hashimoto, T. Uchimoto, and T. Takagi, "Evaluation of detectability of differential type probe using directional eddy current for fibre waviness in CFRP: Advanced Eddy Current Testing for CFRP," Philos. Trans. R. Soc. A Math. Phys. Eng. Sci., vol. 378, no. 2182, Oct. 2020, doi: 10.1098/rsta.2019.0587.
22. R. R. Hughes and S. Dixon, "Performance analysis of single-frequency near electrical resonance signal enhancement (SF-NERSE) defect detection," NDT E Int., vol. 102, pp. 96–103, 2019, doi: 10.1016/j.ndteint.2018.11.008.
23. N. V. Nair et al., "A GMR-based eddy current system for NDE of aircraft structures," IEEE Trans. Magn., vol. 42, no. 10, pp. 3312–3314, 2006, doi: 10.1109/TMAG.2006.879820.
24. K. H. Lee and I. H. Park, "Low frequency eddy current method for internal defect inspection of steel structure," 2012 6th Int. Conf. Electromagn. F. Probl. Appl. ICEF'2012, pp. 1–4, 2012, doi: 10.1109/ICEF.2012.6310321.
25. D. Chen, R. Xie, W. Zhou, H. Hu, and M. Pan, "Multi-channel transimpedance measurement of a planar electromagnetic sensor array," Meas. Sci. Technol., vol. 26, no. 2, 2015, doi: 10.1088/0957-0233/26/2/025102.
26. K. Chen, B. Gao, G. Y. Tian, Y. Yang, C. Yang, and Q. Ma, "Differential Coupling Double-Layer Coil for Eddy Current Testing with High Lift-Off," IEEE Sens. J., vol. 21, no. 16, pp. 18146–18155, 2021, doi: 10.1109/JSEN.2021.3076880.
27. D. Wu, F. Cheng, F. Yang, and C. Huang, "Non-destructive testing for carbon-fiber-reinforced plastic (CFRP) using a novel eddy current probe," Compos. Part B Eng., vol. 177, no. September, p. 107460, 2019, doi: 10.1016/j.compositesb.2019.107460.
28. C. Y. Xiao and J. Zhang, "Analytical solutions of transient pulsed eddy current problem due to elliptical electromagnetic concentrative coils," Chinese Phys. B, vol. 19, no. 12, 2010, doi: 10.1088/1674-1056/19/12/120302.
29. M. Mussatayev, Q. Yi, M. Fitzgerald, V. K. Maes, P. Wilcox, and R. Hughes, "Directional eddy current probe configuration for in-line detection of out-of-plane wrinkles," Compos. Part B Eng., vol. 268, p. 111048, Jan. 2024, doi: 10.1016/j.compositesb.2023.111048.
30. H. Kosukegawa, Y. Kiso, J. Horibe, M. Hashimoto, and T. Takagi, "Electromagnetic Nondestructive Inspection of Fiber Misalignment in CFRP with Directional Eddy Current," 2019, Accessed: Jun. 07, 2022. [Online]. Available: http://www.ndt.net/?id=25069